


## ARTICLE OPEN



# Terrestrial sources of summer arctic moisture and the implication for arctic temperature patterns

Tyler S. Harrington<sup>1</sup> ✉, Jiang Zhu<sup>2</sup> and Christopher B. Skinner<sup>1</sup>

Sea ice melt and ocean heat accumulation in the Arctic are strongly influenced by the presence of atmospheric water vapor during summer. While the relationships between water vapor concentration, radiation, and surface energy fluxes in the Arctic are well understood, the sources of summer Arctic water vapor are not, inhibiting understanding and prediction of Arctic climate. Here we use the Community Earth System Model version 1.3 with online numerical water tracers to determine the geographic sources of summer Arctic water vapor. We find that on average the land surface contributes 56% of total summer Arctic vapor with 47% of that vapor coming from central and eastern Eurasia. Given the proximity to Siberia, near-surface temperatures in the Arctic between 90°E–150°E, including the Laptev Sea, are strongly influenced by concentrations of land surface-based vapor. Years with anomalously large concentrations of land surface-based vapor in the Arctic, and especially in the Laptev Sea region, often exhibit anomalously large near-surface poleward flow from the high latitudes of Siberia, with links to internal variability such as the Arctic Dipole anomaly.

*npj Climate and Atmospheric Science* (2021)4:25; <https://doi.org/10.1038/s41612-021-00181-y>

## INTRODUCTION

Over recent decades, the Earth's average surface air temperature has warmed at a rate of  $\sim 0.2^\circ\text{C decade}^{-1}$ <sup>1</sup>. This warming is unevenly distributed across the planet with the Arctic generally warming at a much quicker rate; a phenomenon referred to as Arctic amplification<sup>2</sup>. Arctic amplification is particularly pronounced during the winter months, with winter warming exceeding that of the summer by nearly a factor of four<sup>3</sup>. However, the enhanced warming rates in winter are largely linked to changes in sea ice extent (SIE), a process that is strongly influenced by the summer climate<sup>4–10</sup>.

Decreased SIE during the summer and fall seasons allows the Arctic Ocean to absorb more solar radiation and increase the ocean heat content<sup>9,11,12</sup>. This accumulation of heat during non-winter months enhances winter Arctic amplification in two ways. First, it limits the pace of sea ice growth in winter, resulting in a greater transfer of ocean heat to the lower atmosphere<sup>9</sup>. Second, the lack of SIE enhances oceanic evaporation, increasing the amount of water vapor in the atmosphere<sup>13,14</sup>. Increases in water vapor have been directly linked to increased downwelling longwave (LW) flux which increases air temperatures and can further limit winter sea ice growth in a positive water vapor feedback process<sup>14</sup>. Consequently, identifying the mechanisms that lead to enhanced sea ice loss during the summer is important not only for summer Arctic warming, but also for winter-time Arctic amplification.

Summer Arctic near-surface temperatures and SIE are strongly influenced by the presence of water vapor and subsequent downward longwave fluxes<sup>15</sup>. Understanding the sources of summer moisture and their variability for the Arctic is therefore critical for the attribution and prediction of Arctic warming patterns. Several studies have attempted to identify the sources of Arctic moisture using Eulerian approaches. Strong moisture transport from the North Atlantic and North Pacific is shown in Jakobson, Vihma<sup>16</sup> with much weaker moisture transport coming

from land masses. Strong poleward moisture flux from the Pacific was also found in Dulfour et al.<sup>17</sup>, while Luo et al.<sup>18</sup> found the North Atlantic to be the strongest source of poleward moisture flux. Though Eulerian approaches have been widely used, Lagrangian techniques are better suited to determine where atmospheric vapor originated from since they are able to specify evaporation source regions<sup>19</sup>.

One popular Lagrangian technique is the use of back-trajectory analysis methods. Several studies have attempted to identify the sources of Arctic moisture using back-trajectories and reanalysis data. Some studies find that atmospheric moisture transport from lower latitude oceanic regions is the dominant source of moisture for the Arctic<sup>20</sup>, while others find the continental regions, namely North America, to dominate summer vapor<sup>21</sup>. While these studies provide a first-order approximation of the sources of summer Arctic moisture, their reliance on back-trajectory analysis methods, which involve an oversimplification of the model physics including a lack of vertical precipitative fluxes, turbulent transfer, and low temporal resolution, potentially biases their estimations of the magnitude and location of moisture sources<sup>22</sup>. Additionally, these studies find conflicting contributions of the land surface to Arctic moisture, which warrants further investigation given rapidly changing land surface characteristics across the globe<sup>23,24</sup>.

Here, we utilize a climate model with online water tracking capabilities to examine the relative roles of different terrestrial and oceanic regions in shaping summer Arctic vapor totals. Our results highlight the key role of the mid- and high-latitude land surface in driving summer Arctic vapor concentrations and the subsequent Arctic warming. Based on these findings, we examine the mechanisms that promote the remote land surface–Arctic climate teleconnection. The quantification of moisture contributions to the Arctic and the controls on this moisture supply are described in “Results” section, and a discussion of the findings in the context of natural modes of variability is presented in “Discussion” section,

<sup>1</sup>Department of Environmental, Earth and Atmospheric Sciences, University of Massachusetts Lowell, Lowell, MA, USA. <sup>2</sup>Climate and Global Dynamics Laboratory, NCAR, Boulder, CO, USA. ✉email: tyler\_harrington2@student.uml.edu

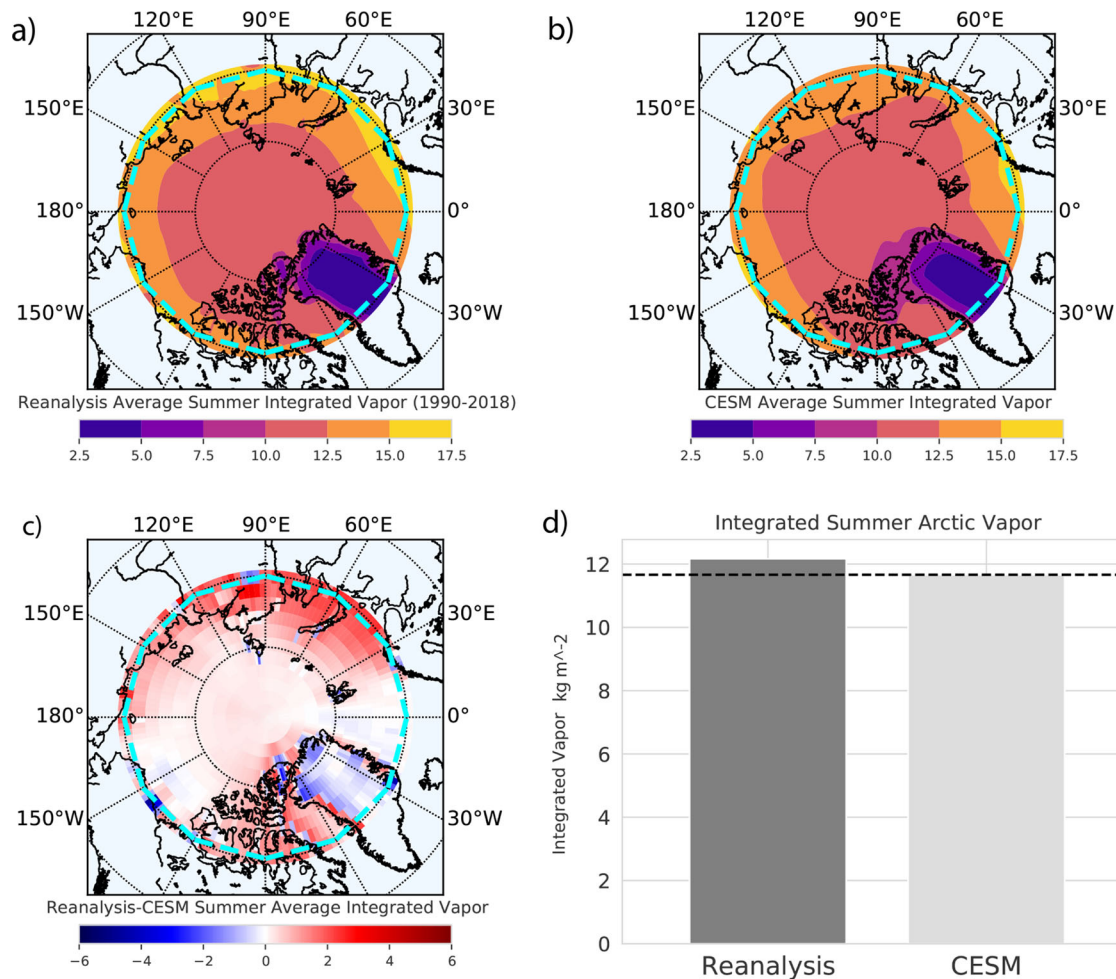


**Fig. 1** Comparison of iCESM-simulated summer integrated vapor to ERA5 reanalysis data. Summer Arctic total integrated vapor from **a** ERA5 reanalysis data, **b** iCESM, and **c** the difference between **a** and **b**. **d** A comparison of the Arctic-averaged total integrated vapor from iCESM and ERA5. Units are in kg m<sup>-2</sup>. The cyan dashed line at 69° latitude marks the Arctic extent used in the area average in **d**.

and the details of the climate model simulation are described in “Methods” section.

## RESULTS

### Comparison of iCESM to ERA5

iCESM slightly underestimates summer average total integrated vapor (TIV) compared with ERA5 reanalysis data (Fig. 1). Summer TIV averaged across the Arctic (north of 69°N) is 11.7 and 12.2 kg m<sup>-2</sup> in iCESM and ERA5, respectively. iCESM simulates the spatial pattern of TIV well, though it slightly underestimates TIV between 30°E-120°E and slightly overestimates TIV over Greenland, which may be the result of differences in resolved topography (Fig. 1c). The overall slight model underestimation of Arctic summer TIV could be the result of using preindustrial atmospheric constituents in CESM, which do not match the present-day concentrations in the reanalysis data. Indeed, the iCESM simulation has an Arctic-average 2-meter air temperature of 272.2 K, 3 K lower than that in ERA5 (275.2 K) (Supplementary Fig. 1). The 2-meter air temperature is higher across the entire Arctic in the reanalysis data, likely explaining a considerable portion of the difference in integrated vapor values between the two datasets. The small difference (<5%) between CESM and ERA5 summer Arctic TIV, and the fact that the TIV differences are likely in large part driven by mean temperature differences between the datasets, supports the use of CESM to investigate Arctic vapor sources and concentrations.

### Breakdown of Arctic vapor sources

There is a distinct seasonal signal of land-based vapor (termed land vapor from this point onward) in the Arctic (Supplementary Fig. 2). During the winter (DJF), the land surface contributes only 9% of total vapor, while it contributes 33% in the spring (MAM), 56% in the summer (JJA), and 33% in the fall (SON). Both the North Atlantic and North Pacific are also important sources of Arctic vapor, contributing 39 and 30% in the winter, 25 and 20% in the spring, 14 and 10% in the summer, and 28 and 20% in the fall, respectively. The other moisture sources examined (Subtropical North Atlantic, Subtropical North Pacific, Arctic, and Other) all have minor roles in all seasons and never contribute more than 9% to total Arctic vapor. Very similar seasonal patterns also exist for both cloud liquid and cloud ice though the North Atlantic dominates winter cloud liquid (Supplementary Table 1).

Given the dominant role of the land surface in shaping summer Arctic vapor (Fig. 2a), sourcing the land vapor to specific regions during this season is necessary for our understanding of Arctic climate and its variability. The HML contribute the most land vapor at 44%, followed by HIL at 35%, LML at 18%, and LOL at 3% (Fig. 2b). Southern Hemisphere land surfaces contribute less than 1% of total Arctic land vapor (not shown). EER and CER contribute the most to summer Arctic land vapor at 27 and 20%, respectively, with WER, ENA, and WNA contributing 16, 18, and 16%, respectively (Fig. 2c). Since the longitude regions are defined between 30°N and 90°N, the “Other” category in Fig. 2c refers to

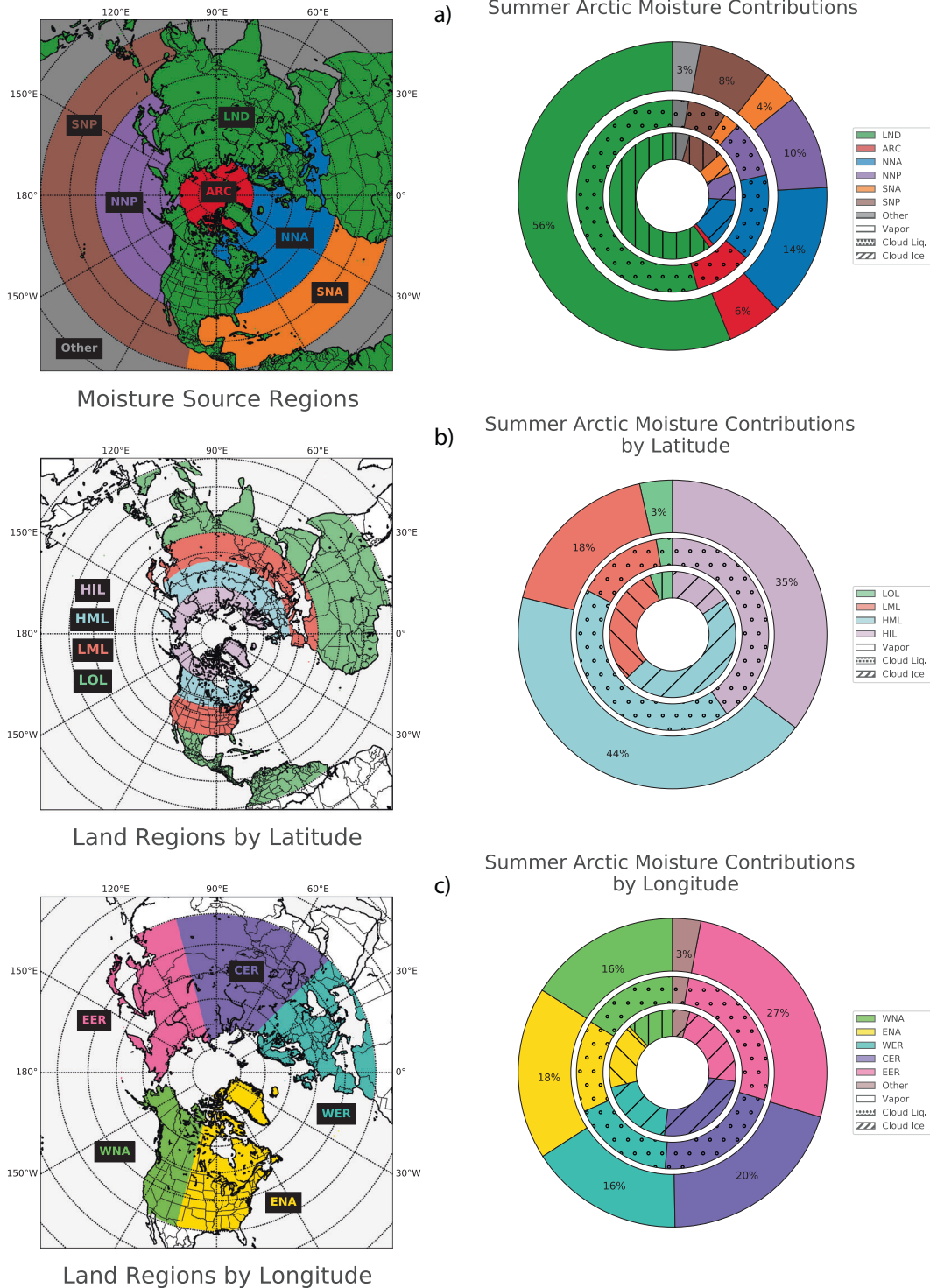


**Fig. 2 Sources of summer Arctic moisture.** **a** Summer Arctic moisture contributions from land and individual ocean regions. **b** Summer Arctic land-based moisture contributions by latitude. **c** Summer Arctic land-based moisture contributions by longitude. Within the pie charts, the outer ring corresponds to water vapor content, the middle ring corresponds to cloud liquid content, and the inner ring corresponds to cloud ice content (units: %).

the LOL vapor from Fig. 2b. A summary of summer vapor contributions from each latitude-defined land region and each longitude-defined land region is provided in Supplementary Tables 2 and 3, respectively. Additionally, each region's contribution to summer cloud liquid and cloud ice is provided in Supplementary Tables 2 and 3.

**Land vapor variability and its connection to Arctic temperatures**

Given the well-established relationship between atmospheric vapor and downwelling radiation, and the dominant contribution of the land surface to summer Arctic vapor content (Fig. 2a), variations in land vapor concentration likely contribute to

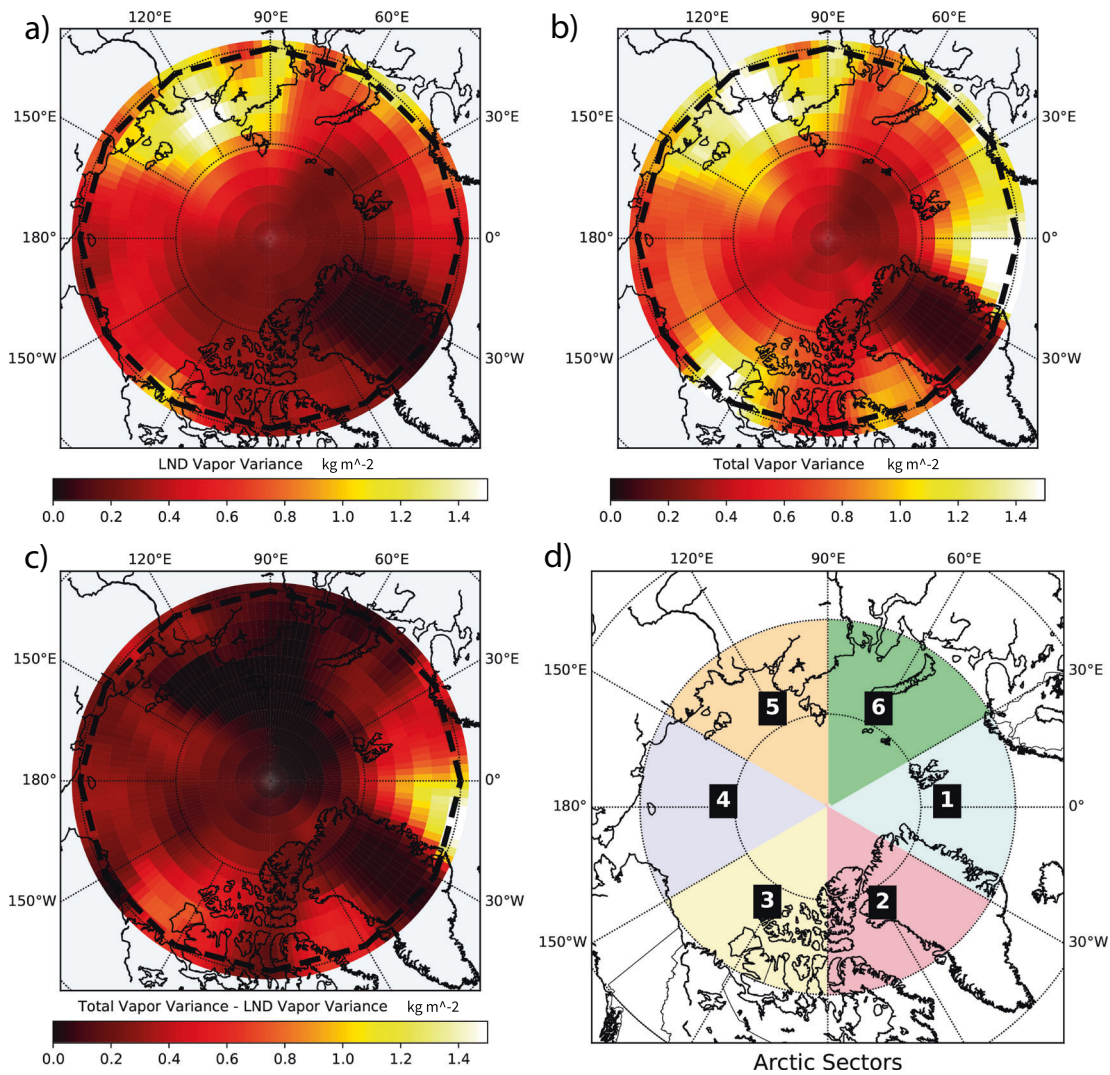


**Fig. 3 Comparison of summer integrated vapor variances.** Variance in **a** integrated land vapor, **b** total integrated vapor, and **c** the difference between **a** and **b**. **d** Definitions of the Arctic sectors to study regional variations in vapor concentration. The black dashed line at 69° latitude marks the Arctic extent. Units are  $(\text{kg m}^{-2})^2$ .

near-surface temperature variability in the Arctic. The variability of summer season vapor over the 29-year period is shown in Fig. 3 with integrated land vapor variance shown in Fig. 3a, total integrated vapor variance in Fig. 3b, and the difference between these two terms (total variance – land variance) in Fig. 3c. The variability in land vapor is not uniform, which suggests that the role of land vapor in shaping Arctic climate may vary considerably for different areas of the Arctic. To further explore the connection between land vapor and temperature in different regions of the Arctic, the Arctic is split into six longitudinal sectors (Fig. 3d): Sector 1 (30°E–30°W), Sector 2 (30°–90°W), Sector 3 (90°–150°W), Sector 4 (150°W–150°E), Sector 5 (150°E–90°E), and Sector 6 (90°E–30°E).

Land vapor variance is most pronounced in Sector 5 (centered around 120°E), an area that encompasses the Laptev Sea and portions of the Kara and East Siberian Seas, with a fairly uniform amount of variance across the rest of the Arctic. The one exception to this is over Greenland. Total vapor variance is less uniformly distributed with maxima occurring in Sectors 1, 3, and 5. The difference between total vapor variance and land vapor variance exhibits a spatial pattern that is similar to the total vapor variance, with local maxima present in Sectors 1 and 3. However, the difference between total vapor variance and land vapor

variance is near zero across all of Sector 5 indicating that changes in land vapor largely dictate changes in total vapor in this region of the Arctic. This also suggests that total vapor in Sectors 1 and 3 is largely controlled by changes in oceanic moisture sources, though a detailed breakdown of these sources is beyond the scope of this paper.

The large contribution of land vapor variance to total vapor variance in Sector 5 suggests temperature in this region in particular may be largely shaped by variations in land vapor concentration. To explore this relationship, and more broadly, the relationship between atmospheric moisture and Arctic temperature, we calculate the correlation between near-surface temperature (at 2 m above the surface) and TIV, integrated land vapor, clouds, and downward surface energy fluxes for the summer season using the 29 years of model simulation. We calculate these correlations for Sector 5 (Figs. 4 and 6) and for the Arctic as a whole (>69°N) (Supplementary Figs. 3 and 5). For model validation, we also calculate the correlation between total integrated vapor and near-surface temperatures in Sector 5 and in the Arctic as a whole from ERA5, which closely match those from iCESM (Supplementary Fig. 4).

The connections between downward LW flux, downward shortwave (SW) flux, TIV, total integrated cloud, and near-surface

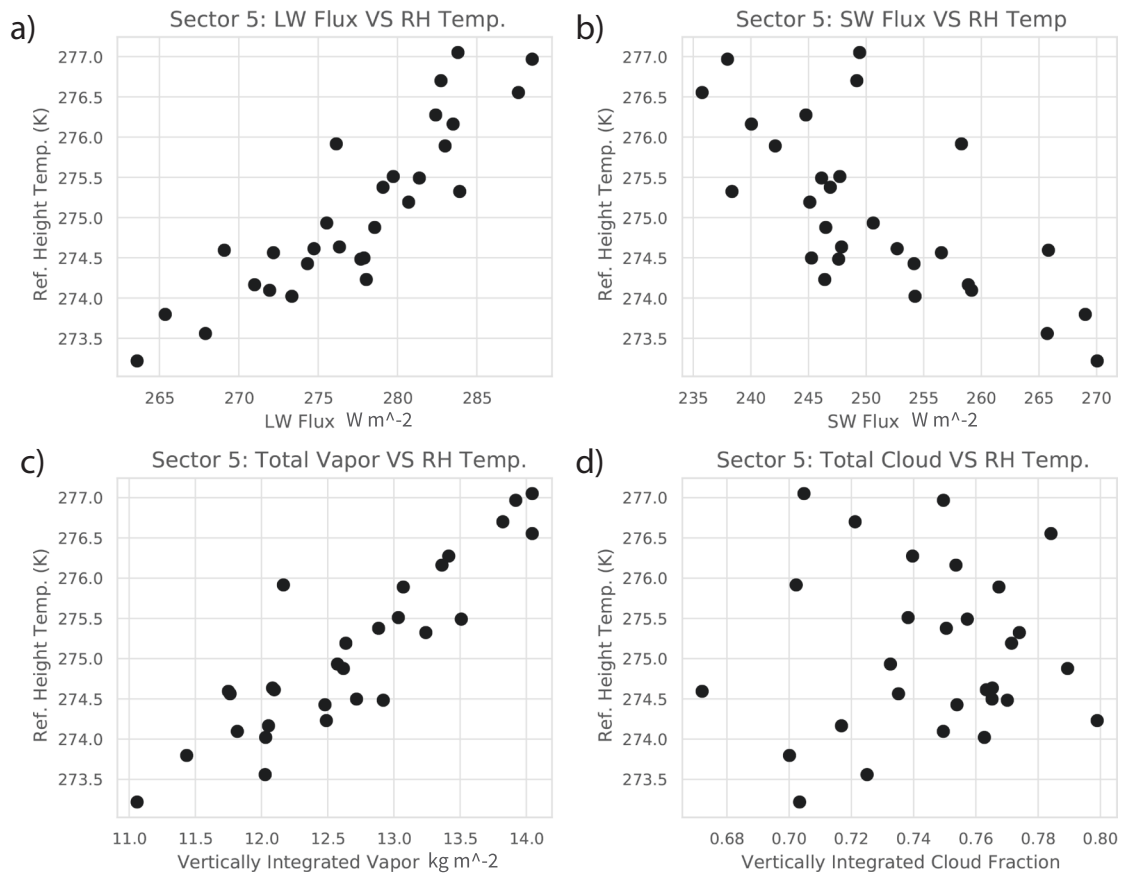


**Fig. 4** Sector 5 near-surface temperature correlation to atmospheric parameters. The relationship between near-surface temperatures and (a) downward LW flux, (b) downward SW flux, (c) TIV, and (d) total integrated cloud in Sector 5 of the Arctic.

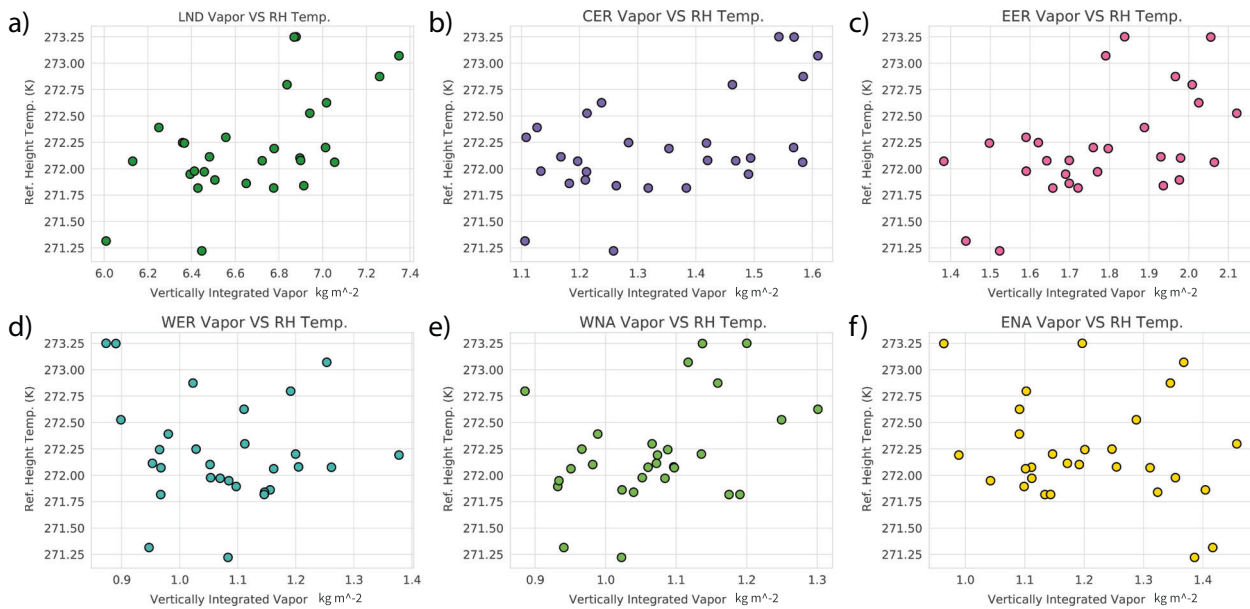


**Fig. 5** Arctic near-surface temperature correlation to land vapor of different source origins. The relationship between near-surface temperatures in the Arctic and (a) vertically integrated land vapor and (b–f) vertically integrated land vapor from each longitudinally defined land region (see Fig. 2). Values are area-averaged north of  $69^{\circ}N$ .

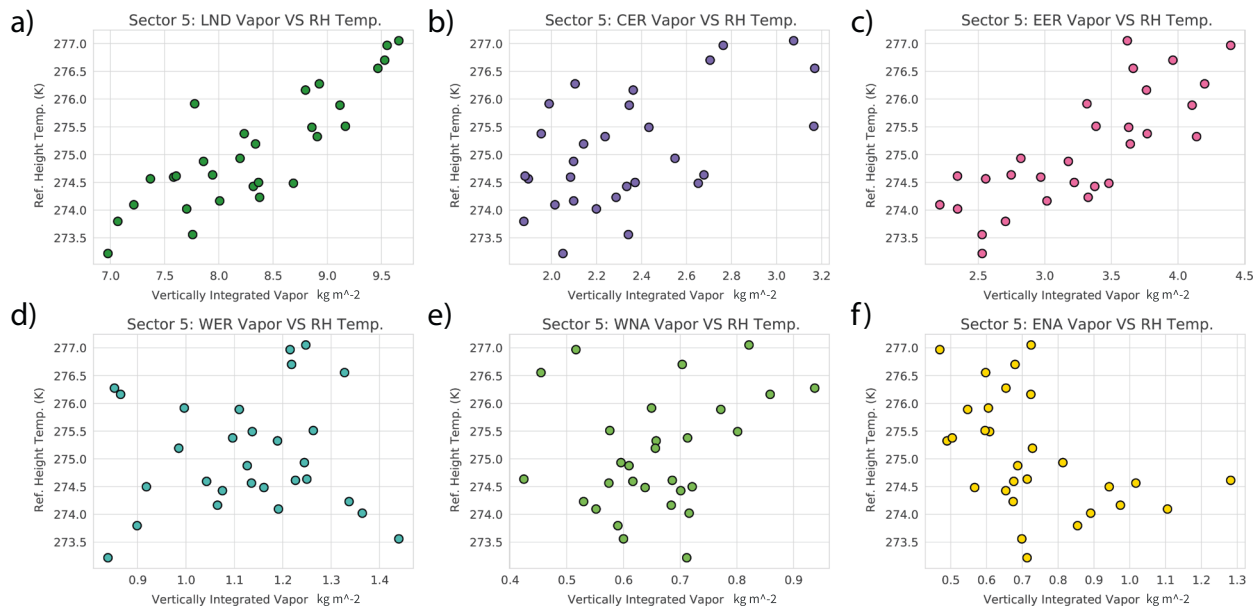


**Fig. 6 Sector 5 near-surface temperature correlation to land vapor of different source origins.** The relationship between near-surface temperatures in Sector 5 and (a) vertically integrated land vapor and (b–f) vertically integrated land vapor from each longitudinally defined land region (see Fig. 2).

temperatures in Sector 5 (Fig. 4) are nearly identical to those for the Arctic as a whole (Supplementary Fig. 3). Specifically, there is a strong positive correlation between surface downward LW flux and near-surface temperatures (adjusted  $R^2$  values of 0.8 for the Arctic and for Sector 5) and between TIV and near-surface temperatures (adjusted  $R^2$  values of 0.7 for the Arctic and 0.8 for Sector 5), a negative correlation between SW flux and near-surface temperatures (adjusted  $R^2$  of 0.4 for the Arctic and 0.5 for Sector 5), and no correlation between total integrated cloud fraction and near-surface temperatures, consistent with the findings of Middlemas et al.<sup>25</sup> However, the relationship between land vapor and near-surface temperatures is much stronger in Sector 5, with adjusted  $R^2$  values increasing from 0.3 for the Arctic as a whole (Fig. 5a) to 0.7 for Sector 5 (Fig. 6a).

Near-surface temperatures in Sector 5 correlate especially well with variations in land vapor from the CER and EER regions, with adjusted  $R^2$  values of 0.3 and 0.6, respectively (Fig. 6b, c). There is little to no correlation between WER, ENA, or WNA vapor and near-surface temperatures in Sector 5 (Fig. 6d–f). Additionally, the relationships between the vapor sourced from any of the individual longitudinally defined land regions and Arctic-averaged near-surface temperatures are weak (Fig. 5), with the best relationship being EER with an adjusted  $R^2$  value of 0.2 (Fig. 5c). Given the somewhat stronger relationship between temperature and total land vapor in the Arctic as a whole (Fig. 5a), the weak relationships between Arctic-averaged temperatures and individual longitudinally defined regions suggest that anomalous fluxes from multiple regions simultaneously may be required to strongly influence Arctic-wide temperatures.

The importance of land vapor as a control on temperatures in Sector 5 is further investigated by comparing anomalously high and low land vapor years (Supplementary Fig. 5). The three highest and lowest integrated land vapor years in Sector 5 are selected using the 0.90 and 0.10 quantiles. Temperatures from those years are then averaged and subtracted from the climatological summer mean temperatures to examine the anomalies. In years with the highest (lowest) amounts of land vapor in Sector 5, near-surface temperatures are higher (lower) than the climatological mean, further demonstrating the importance of understanding land vapor transport into the Arctic. While

the most intense warming (cooling) is located within Sector 5, the warming (cooling) patterns are not confined solely to this one sector. This indicates that the processes that result in large anomalies in land vapor (and subsequent temperature changes) over Sector 5 can also have Arctic-wide impacts on temperature.

#### Atmospheric controls on region-specific land vapor

The direct link established between land vapor and Arctic warming, particularly within Sector 5, highlights the crucial role of land vapor and its variability in regulating Arctic climate. The climatological summer land vapor average across the Arctic is  $\sim 6.6 \text{ kg m}^{-2}$  with a variance of  $0.10 \text{ (kg m}^{-2}\text{)}^2$ . The variations in land vapor are driven by terrestrial evapotranspiration (ET) fluctuations and/or changes in atmospheric circulation patterns, the latter of which is the focus here. Given the especially large influence of the EER region on summer Arctic vapor (Fig. 2c), and the strong correlation between EER vapor content and warming in Sector 5 (Fig. 6c), the analysis of EER vapor variability is highlighted in the main text (Figs. 7 and 8), while figures of the other four regions are shown in the Supplementary.

For each longitudinally defined land region, a time series of region-specific summer land vapor averaged across the Arctic is shown, with anomalous high and low vapor contribution summers highlighted with red and blue stars, respectively (Fig. 7a, and Supplementary Figs. 6–9a). Below each region's time series are the corresponding average sea-level pressure (SLP) and 500 mb geopotential height (GPH) fields/anomalies for the high and low vapor summer composites (Fig. 7b–d, and Supplementary Figs. 6–9b–d). Years are selected as anomalous when region-specific vapor exceeds (falls short of) the mean + (–)  $0.15 \times \text{mean}$ . Anomalies are selected this way because the variance in vapor from the different land regions varies substantially (Supplementary Fig. 10), and not all of the vapor sources are normally distributed (Supplementary Fig. 11). Unlike the use of quantiles, this method guarantees that the selected cases are far enough away from the mean to be considered an anomaly. The use of standard deviation classes were considered, but the bimodally-distributed CER region prevented any one standard deviation classifier from capturing all anomalies in all regions.

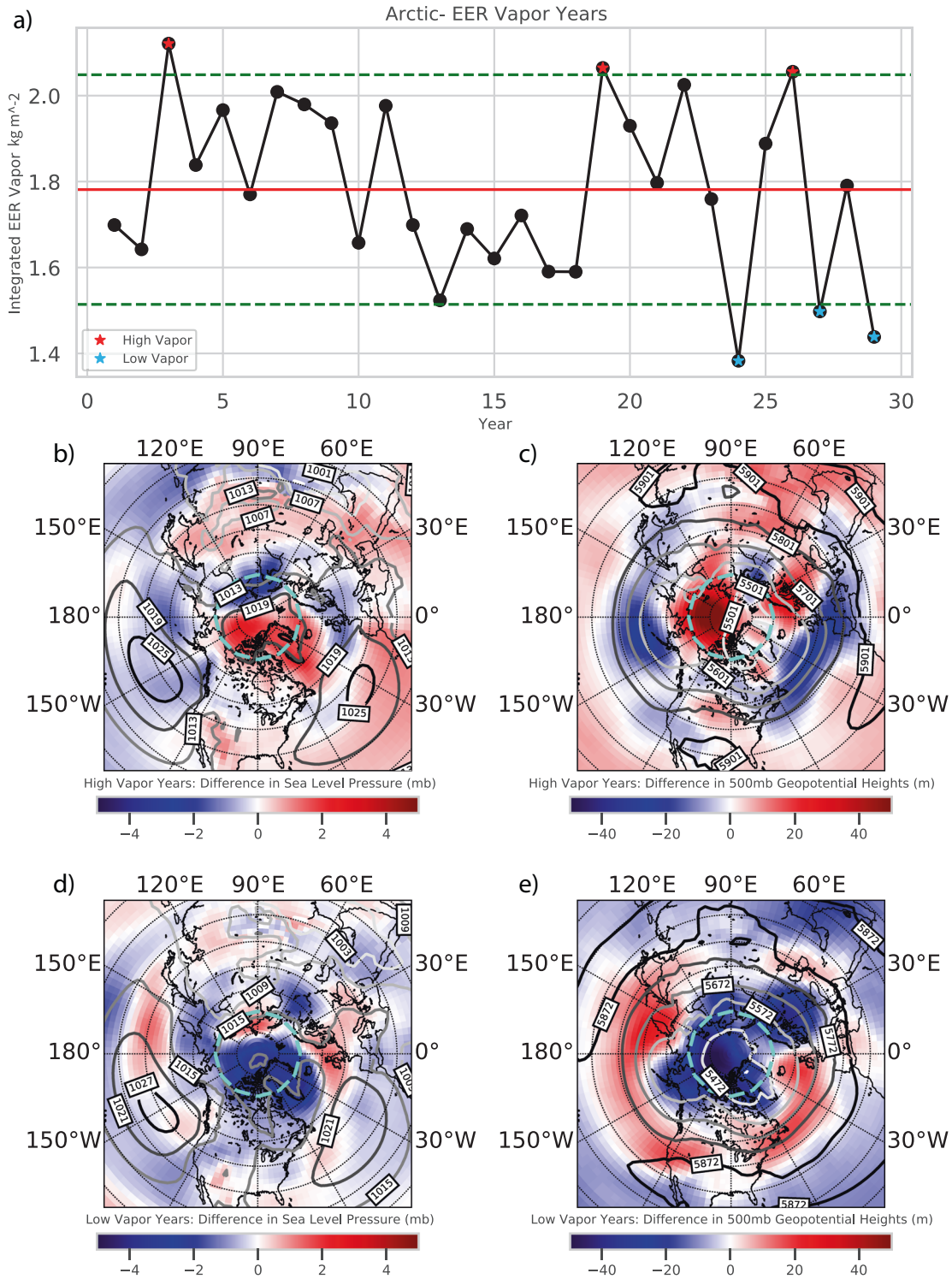


**Fig. 7 Atmospheric conditions associated with anomalous poleward EER vapor transport.** **a** Mean summer EER vapor in the Arctic for each year of the simulation. The red stars denote anomalously high vapor years used in panels **b** and **c**, and the blue stars denote anomalously low vapor years used in panels **d** and **e**. **b** Average SLP fields (contours) and the difference from the climatological mean (shading) for high vapor anomaly years. **c** Average 500 mb GPH fields (contours) and the difference from the climatological mean (shading) for high vapor anomaly years. **d** Average SLP fields (contours) and the difference from the climatological mean (shading) for low vapor anomaly years. **e** Average 500 mb GPH fields (contours) and the difference from the climatological mean (shading) for low vapor anomaly years. The cyan dashed line at 69° latitude marks the Arctic extent used in the area average in **a**.

The composite SLP patterns reveal anomalous land moisture transport into the Arctic is largely influenced by lower atmospheric pressure patterns in and surrounding the Arctic. Several coherent and consistent SLP features stand out across the

different regions, though, as will be shown next, various different atmospheric patterns are able to promote and suppress land vapor transport from a specific region. The composite analysis reveals that negative SLP anomalies along or very near a particular

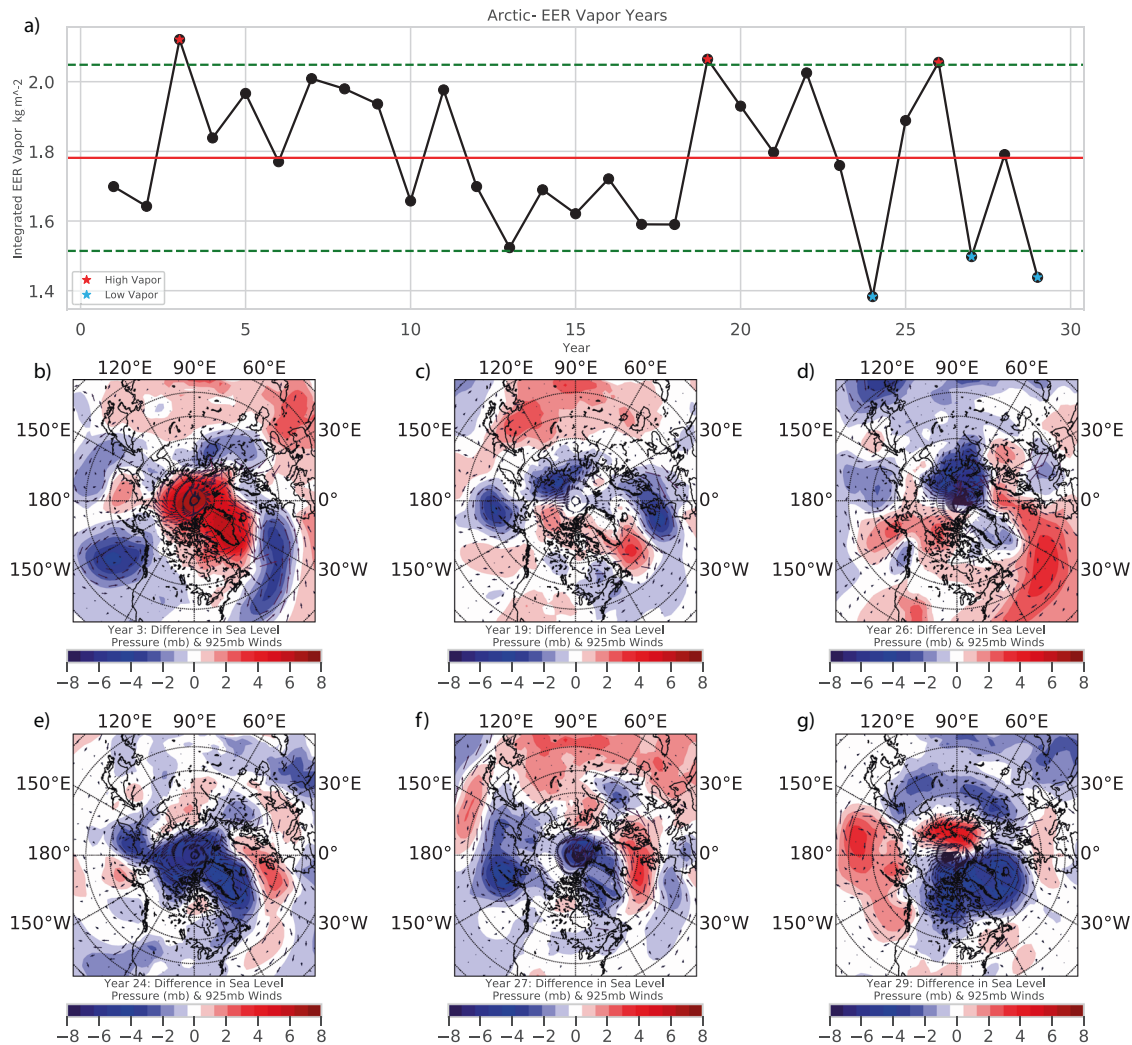


**Fig. 8** SLP conditions associated with anomalous poleward EER vapor transport. **a** Mean summer EER vapor in the Arctic for each year of the simulation. The red stars denote anomalously high vapor years used in panels **b** and **d**, and the blue stars denote anomalously low vapor years used in panels **e–g**. **b** Year 3 SLP and 925 mb wind anomaly, **c** Year 19 SLP and 925 mb wind anomaly, **d** Year 26 SLP and 925 mb wind anomaly, **e** Year 24 SLP and 925 mb wind anomaly, **f** Year 27 SLP and 925 mb wind anomaly, and **g** Year 29 SLP and 925 mb wind anomaly.

region's side of the Arctic can promote high vapor contributions from that region. For example, for the two largest contributors to Arctic land vapor, EER and CER, lower than normal SLP on the central/eastern Eurasian side of the Arctic near 70°N drives enhanced CER- and EER-based vapor to the Arctic (Fig. 7b and Supplementary Fig. 6b). Similar negative SLP anomalies in the composites are found northwest of the United Kingdom towards the Norwegian Sea in high WER vapor summers (Supplementary Fig. 7b), over the Canadian Archipelago and Greenland during high ENA vapor summers (Supplementary Fig. 8b), and over Alaska during high WNA vapor summers (Supplementary Fig. 9b). The composite analysis reveals that the SLP features associated with anomalously low vapor years are slightly less consistent across regions, though positive SLP anomalies near the region of interest are commonly seen. For example, strong positive SLP anomalies over Iceland and the Greenland Sea are associated with low land vapor from WER (Supplementary Fig. 7d), while strong positive SLP anomalies over Alaska and the Beaufort Sea are associated with low land vapor from WNA (Supplementary Fig. 9d). For EER, CER, and ENA, positive SLP anomalies are located at the northern extent of each continental region, for example, over northern Siberia and the Laptev Sea near 90°E for EER (Supplementary Fig. 7d), over northern Siberia and the Kara Sea

near 60°E for CER (Supplementary Fig. 6d), and over the Canadian Archipelago and Quebec for ENA (Supplementary Fig. 8d), but they are fairly weak.

Given the low number of summers used in the composites of extreme high and low vapor anomaly years, we examine each of the individual summers from the composites to better identify the seasonal atmospheric features that promote land vapor anomalies and to assess the robustness of the patterns revealed in the composite analysis. Our focus here is on the SLP anomalies and associated lower atmospheric wind anomalies (Fig. 8 and Supplementary Figs. 12–15), which, as will be shown, strongly influence land vapor transport. For the EER region, two of the three high vapor summers (years 19 and 26) closely resemble one another (and the composite) with lower than average SLP on the Eurasian side of the Arctic (centered between 60°E and 120°E along the coast of the Kara and Laptev Seas) and associated winds that promote moisture advection from EER (Fig. 8c, d). However, the third year (year 3) deviates from the other two years (Fig. 8b). Though negative SLP anomalies are still present along the northern Siberian land surface, a prominent positive SLP anomaly exists across most of the Arctic during the summer. Based on the SLP and low-level winds alone, year 3 would not be expected to exhibit the highest Arctic EER vapor in the simulation (Fig. 8a). The



anticyclonic winds around the high direct air over EER slightly away from the Arctic. However, high-latitude ( $>60^{\circ}\text{N}$ ) EER ET is greater in year 3 than any other year of the simulation (Supplementary Fig. 17a). This suggests that while lower atmospheric pressure and winds largely control the flux of EER vapor into the Arctic, regionally high anomalies of ET can overcome less than ideal atmospheric circulation conditions to promote high Arctic vapor anomalies.

The low EER vapor years also reveal that several different mechanisms can limit the concentration of EER vapor in the Arctic (Fig. 8e–g). In year 29, the strong positive SLP anomaly and anticyclone flow over the Laptev and Kara Seas, directs EER moisture away from the Arctic, as was discussed for the composite pattern (Fig. 8g). However, the positive SLP anomalies in this region in years 24 and 27 are very weak, and the primary control on reduced EER vapor in the Arctic appears to be the equatorward flow along the western flank of a negative SLP anomaly centered over the Bering Sea (Fig. 8e–f).

The SLP anomalies conducive for high EER vapor transport into the Arctic are similar for the CER region as well. For the years with extreme positive anomalies of CER vapor in the Arctic, four of the five cases exhibit lower than normal SLP across the Eurasian side of the Arctic (centered at  $90^{\circ}\text{E}$ ) with associated poleward-directed winds from CER (Supplementary Fig. 12), consistent with the composite analysis (Supplementary Fig. 6b). However, year 28 demonstrates that other atmospheric features can also enhance vapor transport from CER (Supplementary Fig. 12f). Like the other high CER vapor years, year 28 exhibits negative SLP anomalies just north of the CER region (near  $45^{\circ}\text{E}$ ) which promote cyclonic circulation and enhanced winds from CER. However, during this summer, high-pressure across much of the CER region (centered at  $60^{\circ}\text{N}$ ,  $70^{\circ}\text{E}$ ) strongly enhances northward flow through the CER region into the Arctic (Supplementary Fig. 12f). Additionally, year 28 high-latitude CER ET is anomalously high (Supplementary Fig. 16b). This suggests that while the SLP conditions shown in the composite analysis for CER (Supplementary Fig. 6b) lead to enhanced CER vapor in the Arctic, other anomalous circulation patterns with poleward-directed winds, especially when combined with positive ET anomalies can have a similar effect on the flow of CER vapor into the Arctic. Low CER vapor years consistently exhibit a positive SLP anomaly just west of the CER region, or along the Laptev Sea/Kara Sea, both of which drive winds from the CER away from the Arctic (Supplementary Figs. 12g–j). Because these positive SLP anomalies are located in slightly different regions in some years, when compositing these years together, the average composite SLP values are fairly weak (Supplementary Fig. 6d). However, a positive SLP anomaly is always close to the region.

While not discussed in detail here, the individual cases for high and low vapor from WER (Supplementary Fig. 13), ENA (Supplementary Fig. 14), and WNA (Supplementary Fig. 15) also largely match their respective composite analysis patterns, though exceptions can occur for those regions as well (Supplementary Figs. 13–15). For example, all three low-WER vapor summers exhibit low-level anticyclonic circulation preventing the transport of WER vapor into the Arctic (though the exact positioning of the high-pressure anomaly in the North Atlantic varies) (Supplementary Fig. 13), all high ENA vapor years exhibit large negative SLP and cyclonic circulation anomalies near Greenland (Supplementary Fig. 14), and both anomalously high WNA vapor years exhibit cyclonic circulation anomalies in the Gulf of Alaska (Supplementary Fig. 15).

The dipole structure of SLP anomalies associated with high and low land vapor years from several of the continental regions (e.g., EER and ENA) resembles that of the Arctic Dipole anomaly, defined as the second empirical orthogonal function (EOF) of mean JJA SLP north of  $70^{\circ}\text{N}$  (Supplementary Figs. 17 and 18)<sup>26,27</sup>. For example, the composite of JJA SLP during the extreme positive phase of the Arctic Dipole (summers in which the first principle

component PC1 exceeds 1 standard deviation) exhibits negative SLP north of Siberia, and positive SLP along the Canadian Arctic (Supplementary Fig. 18), consistent with the composite SLP pattern that promotes land vapor from EER (Fig. 7b). Indeed, two of the three highest EER vapor years in the Arctic (years 19 and 26) are extreme positive Arctic dipole years (as noted previously, year 3 is a high EER vapor year due to extreme ET anomalies). Likewise, the three summers with the highest Arctic vapor sourced from ENA (years 1, 18, and 29) (Supplementary Fig. 14) coincide with negative Arctic Dipole years, a result of anomalously low SLP anomalies on the Canadian Archipelago side of the Arctic.

The composite analysis of 500 mb GPH fields also reveals similar patterns associated with land vapor transport among the different regions. The axis of orientation of the 500 mb GPH fields also help govern the flow of anomalous land moisture transport into the Arctic. For both EER and CER, high (low) vapor anomalies are associated with the 500 mb GPH fields (contours) aligning along the  $90^{\circ}\text{E}$ – $90^{\circ}\text{W}$  axis ( $120^{\circ}\text{E}$ – $60^{\circ}\text{W}$  axis). In contrast, WER and ENA high (low) vapor anomalies are accompanied by 500 mb GPH fields aligning along the  $120^{\circ}\text{E}$ – $60^{\circ}\text{W}$  axis ( $90^{\circ}\text{E}$ – $90^{\circ}\text{W}$  axis). WNA is the only region without a clear 500 mb GPH field signal, though this could be attributed to the limited number of years used in the creation of the anomalies due to the lack of variance in WNA vapor.

### Controls on total Arctic land vapor

Though the strongest influence of land vapor on Arctic temperatures is found in Sector 5, the positive correlation between land vapor and Arctic-averaged temperature warrants further investigation of the conditions that control Arctic-wide land vapor anomalies. To determine which land regions and corresponding atmospheric circulation patterns regulate total Arctic land vapor, we examine the conditions associated with the highest (Fig. 9) and lowest (Fig. 10) concentrations of land vapor in the Arctic. Years where the total land vapor averaged across the Arctic are above (below) the 0.90 (0.10) quantiles are considered anomalously high (low) land vapor years (Figs. 9a and 10a). Averaged across the high (low) land vapor anomaly cases, vapor increases (decreases) by over  $0.5\text{ kg m}^{-2}$  above (below) the summer average, and contributes 60% (54%) of the total Arctic vapor (Figs. 9b and 10b). The gains/losses in Arctic land vapor are largely attributed to changes in vapor from the EER, CER, HML, and HIL regions (Figs. 9c, d, and 10c, d). Anomalous contributions from the ocean regions during high and low land vapor years are generally small, though in aggregate they slightly counteract the land vapor anomalies (Figs. 9e and 10e). For the high (low) land vapor anomaly composites, SLPs are lower (higher) than average on the central/eastern Eurasian side of the Arctic and the GPH fields align along the  $90^{\circ}\text{E}$ – $90^{\circ}\text{W}$  axis ( $120^{\circ}\text{E}$ – $60^{\circ}\text{W}$  axis) (Figs. 9g, h, and 10g, h). Indeed, the atmospheric patterns that promote large land vapor anomalies from the EER region often resemble those from the CER region, and contributions from the two are often positively correlated with one another, though the correlation is relatively weak (Supplementary Fig. 19).

To assess whether the Arctic-wide vapor anomalies are driven by coherent patterns in anomalous ET fluxes, we examine the summer season ET fluxes in the high and low Arctic land vapor years. The ET anomalies in the regions with the largest land vapor contribution changes, EER and CER, are relatively small ( $<1\%$  difference for EER and CER HIL/HML regions) and spatially heterogeneous in both the low and high vapor cases, suggesting only a minor role for mid and high-latitude ET anomalies in shaping Arctic vapor. Though, it is worth noting that, though small, the composite ET anomalies along the high latitudes of Siberia are anomalously high (low) in high (low) Arctic land vapor years (Figs. 9f and 10f), and as noted previously, summers with

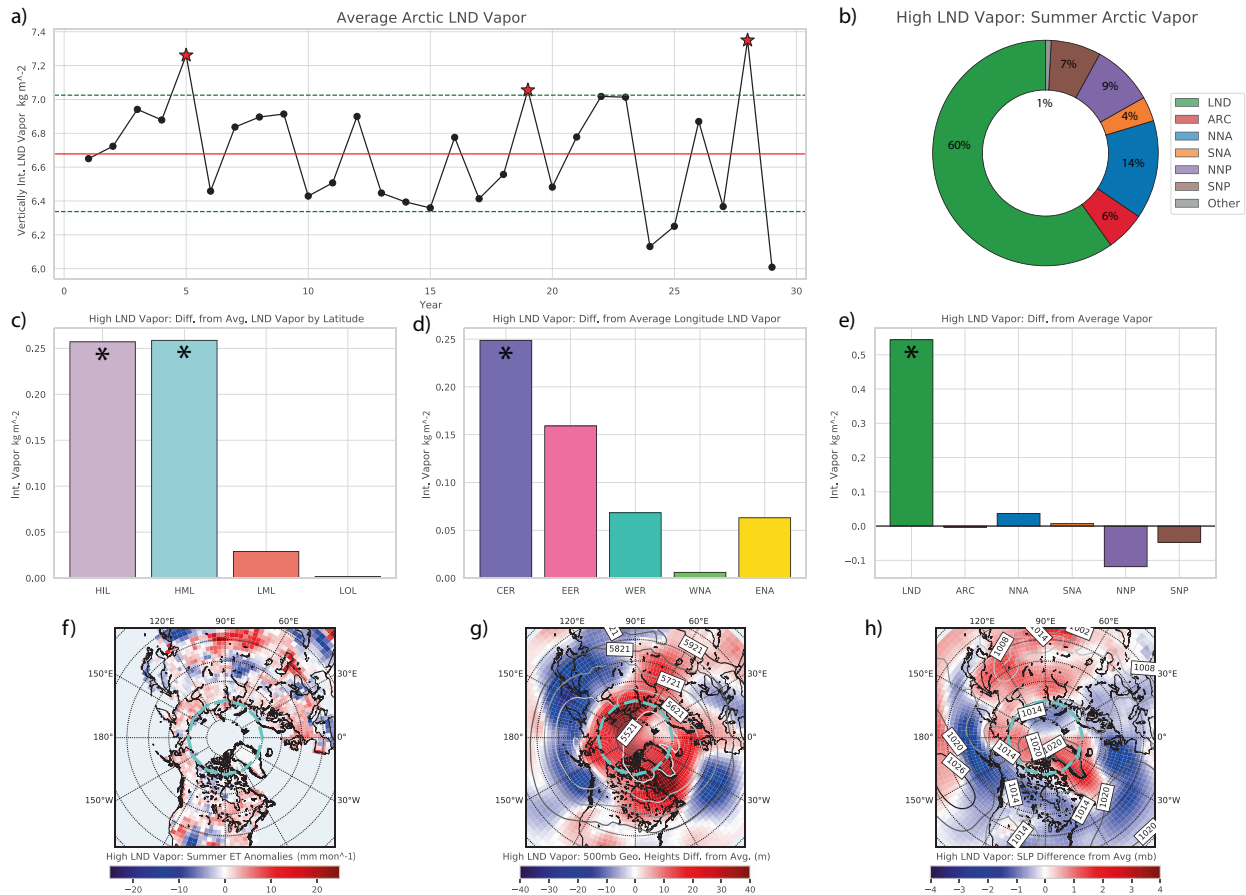


**Fig. 9** Conditions associated with the largest positive anomalies of land vapor in the Arctic. **a** Average summer land vapor in the Arctic for each year of the simulation. The red stars denote anomalously high land vapor years used in panels **b–h**. **b** The percent contribution to total Arctic vapor from land and individual ocean regions in anomalously high land vapor summers. **c** The anomalies in land vapor contributions from latitude-based regions during high Arctic land vapor summers. **d** The anomalies in land vapor contributions from longitude-based regions during high Arctic land vapor summers. **e** The anomalies in vapor contributions from land and individual ocean regions during high Arctic land vapor summers. **f** The anomalies in ET during high Arctic land vapor summers. **g** The average 500 mb GPH fields (contours) and difference from climatological mean (shading) during high Arctic land vapor summers. **h** The average SLP fields (contours) and difference from climatological mean (shading) during high Arctic land vapor summers. Asterisks on the bars in **c–e** indicate statistically significant anomalies (see Methods).

extreme ET anomalies, especially in the high latitudes, can drive substantial anomalies in land vapor from specific regions.

## DISCUSSION

The online water tracer simulation presented here indicates that the land surface provides on average 56% of all summer season vapor in the Arctic in CESM1.3. The land surface also contributes substantially to Arctic vapor concentrations during the spring (33%) and fall (33%) seasons (Supplementary Fig. 2), though detailed analysis of the processes that shape this land-Arctic teleconnection in those seasons is left for future work. The water tracers reveal that most (79%) summer land-based moisture in the Arctic is sourced from latitudes poleward of 45°N and that central and eastern Eurasia contribute more moisture (20 and 27%) than western Eurasia, western North America, or eastern North America (16, 16, and 18%) (Fig. 2b, c). These findings indicate central and eastern Eurasia play the most important role in supplying Arctic summer vapor and in regulating subsequent summer Arctic warming and sea-ice melt.

The composite SLP patterns suggest pressure conditions in and near the Arctic are an important factor regulating poleward land moisture flux into the Arctic (Figs. 7 and 8 and Supplementary Figs. 6–13). In general, when there are positive SLP anomalies just

north of the land region of interest, the strong outward flow away from the high SLP anomaly prevents land moisture from reaching the Arctic. Additionally, anomalous land vapor contributions from CER and EER are often driven by similar changes to the strength and position of Arctic SLP anomalies (Figs. 7 and 8, Supplementary Figs. 6 and 7). Lower than normal SLPs across the central and east Eurasian side of the Arctic allows more low-level moist air from these land masses to reach the Arctic. The overlap in the ideal Arctic SLP conditions for the poleward flux of EER and CER vapor contributes to a weak, positive correlation between the two vapor sources (Supplementary Fig. 19). The SLP patterns associated with enhanced moisture flux from one region are also associated with inhibited moisture flux from another. For example, higher than average SLPs along the northern edge of CER and EER are often found with negative SLP anomalies along the Canadian side of the Arctic. These patterns are associated with inhibited CER vapor flux and enhanced ENA vapor flux (Fig. 7d, Supplementary Figs. 6d and 8a). The opposing effects SLP anomalies have on different land masses depending on their location likely helps to constrain the variability of total land vapor in the Arctic, and leads to relatively weak, negative correlations between EER/CER and ENA Arctic vapor contributions (Supplementary Fig. 19). Despite Arctic SLP conditions enhancing the flux of land vapor from some land source regions while simultaneously inhibiting the flux from

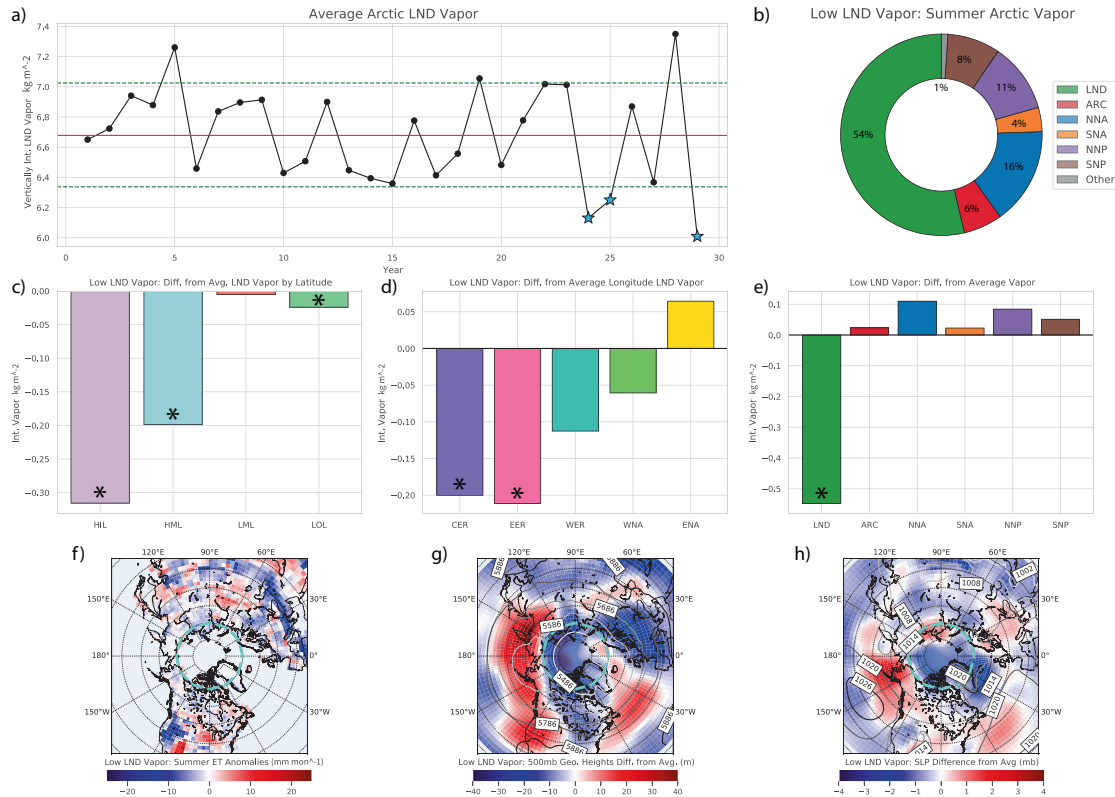


**Fig. 10** Conditions associated with the largest negative anomalies of land vapor in the Arctic. **a** Average summer land vapor in the Arctic for each year of the simulation. The blue stars denote anomalously low land vapor years used in panels **b–h**. **b** The percent contribution to total Arctic vapor from land and individual ocean regions in anomalously low land vapor summers. **c** The anomalies in land vapor contributions from latitude-based regions during low Arctic land vapor summers. **d** The anomalies in land vapor contributions from longitude-based regions during low Arctic land vapor summers. **e** The anomalies in vapor contributions from land and individual ocean regions during low Arctic land vapor summers. **f** The anomalies in ET during low Arctic land vapor summers. **g** The average 500 mb GPH fields (contours) and difference from climatological mean (shading) during low Arctic land vapor summers. **h** The average SLP fields (contours) and difference from climatological mean (shading) during low Arctic land vapor summers. Asterisks on the bars in **c–e** indicate statistically significant anomalies (see Methods).

others, summer land vapor still varies considerably from year to year. While not directly shown in this simulation, since SLPs most directly impact low-level atmospheric circulation patterns, land vapor fluctuations due to changes in SLP conditions are most likely from the HIL region. Since HIL contributes 35% of total Arctic land vapor during the summer (Fig. 2b), SLP anomalies have a notable control on land vapor fluctuations.

Most of the individual high and low anomaly years used in the SLP composites resemble one another (and the SLP conditions of the composites) (Fig. 8 and Supplementary Figs. 12–15). Two of the three high EER vapor anomaly years (Fig. 8) and four of the five high CER vapor anomaly years (Supplementary Fig. 12) exhibit the same SLP anomalies as their respective composites with below average SLPs on the Eurasian side of the Arctic. While these SLP conditions are present in most of the individual years, there are a couple exceptions in which other mechanisms also exhibit an influence on vapor anomalies in the Arctic, namely year 3 for EER (Fig. 8b) and year 28 for CER (Supplementary Fig. 12f). In year 3, positive SLP anomalies are present across much of the Arctic, along with a relatively weak negative SLP anomaly (in comparison to years 19 and 26) just above Eurasia. Similarly, year 28 has above normal SLPs across much of the Eurasian side of the Arctic, and relatively weak negative SLP anomalies near 45°E. Both of these years have Arctic SLP conditions that do not strongly support enhanced poleward transport of vapor from the EER and CER regions. However, the year 3 high-latitude (>60°N) EER ET is the highest of any model year simulation (Supplementary Fig. 16a),

and the year 28 high-latitude CER ET is anomalously high as well (Supplementary Fig. 16b). There is also a strong region of high pressure across the CER region during year 28 promoting enhanced poleward flow from the northern portions of CER into the Arctic (Supplementary Fig. 12f). These two outlier years show that while the composite SLP conditions are ideal for enhanced flow of EER/CER vapor into the Arctic, positive ET anomalies and other anomalous circulation features enhancing poleward flow can overcome less than ideal Arctic SLP conditions and lead to anomalously high EER/CER vapor concentrations.

The composite 500 mb GPH fields also point to a key atmospheric control on Arctic land vapor fluctuations. As with the SLP anomalies, there are 500 mb GPH field characteristics with opposing consequences for different land masses. For both EER and CER, high (low) land moisture anomalies are present when the 500 mb GPH fields align along the 90°E–90°W axis (120°E–60°W axis) (Fig. 7 and Supplementary Fig. 6). The alignment along the 90°E–90°W axis allows atmospheric waves to penetrate the Arctic circle and supply the Arctic with land vapor from EER and CER. The opposite is true for WER and ENA with high (low) anomalies associated with GPH fields aligned along the 120°E–90°W axis (90°E–90°W axis) (Supplementary Figs. 7 and 8). These opposing responses to 500 mb GPH fields for different regions also help to limit total Arctic land vapor variability. The 500 mb GPH fields likely regulate the flow of land moisture from lower latitudes into the Arctic due to vertical mixing as moisture travels poleward. The additional time spent in the atmosphere to reach the Arctic allows

lower latitude land moisture to distribute to higher vertical levels of the atmosphere. The leading latitude moisture contributor, HML, is presumably most directly influenced by changes in 500 mb GPH fields. Future work with archived daily-scale atmospheric data will allow us to directly link synoptic wave variability with moisture fluxes into the Arctic.

The atmospheric conditions corresponding to the largest anomalies in total Arctic land vapor parallel the necessary atmospheric conditions for anomalies in CER and EER vapor as shown in the composite analysis (Fig. 7 and Supplementary Fig. 6). Indeed nearly all of the years with high total Arctic land vapor coincide with years of high EER and/or CER vapor. Almost all of the additional land vapor entering the Arctic during anomalously high vapor years is sourced from either HIL or HML further indicating that SLPs largely control HIL vapor and GPH fields control HML vapor. For the anomalously high Arctic land vapor years, SLPs are lower than normal on the central and east Eurasian side of the Arctic and the 500 mb GPH fields align along the 90°E-90°W axis (Fig. 9). This pattern emerges during the positive phase of the Arctic Dipole (AD) anomaly<sup>27–29</sup>. Studies have suggested the circulation anomalies associated with the positive AD phase enhance heat and moisture transport to the Arctic from the North Pacific<sup>30</sup>, but the role this mode of variability has on transporting land-sourced vapor has not been explored. The moisture tracking analysis presented here suggests the positive (negative) AD phase provides the optimal atmospheric conditions for enhanced EER/CER (ENA) poleward flow, thus enhancing total Arctic land vapor (Fig. 9 and Supplementary Fig. 18). While the positive (negative) AD phase closely matches the composite SLP and GPH conditions for enhanced EER/CER (ENA) vapor, given the simultaneous occurrence of other modes of variability (e.g., the Arctic Oscillation), and ET anomalies, not all positive and negative Arctic Dipole years induce anomalously high and low land vapor advection from these continental regions. However, the connection between the AD anomaly and anomalous land vapor transport from the high moisture region of EER may help to explain anomalously warm conditions in the Arctic during some positive AD years.

The magnitude of land vapor fluctuations varies considerably across the Arctic with the largest variations occurring in Sector 5 (90°E-150°E) (Fig. 3). Land vapor increases in this sector are directly linked to increases in LW flux and near-surface temperatures (Fig. 4, Supplementary Figs. 4 and 5). Given the proximity of this sector to the eastern and central Eurasian land masses, which have a key role in Arctic vapor concentrations, climate in Sector 5 is especially sensitive to atmospheric circulation that promotes/inhibits flow from EER/CER. A positive trend in summer vapor across this portion of the Arctic due to summertime, circulation-driven, moist air transport was also noted in Rinke et al.<sup>31</sup>. Among other mechanisms, the AD may be an important regulator of Sector 5 land vapor and hence temperature variability. This finding is consistent with other studies that have connected the positive phase of the AD to enhanced LW flux across much of Sector 5<sup>30</sup>. Additionally, the enhanced LW flux from anomalously high Arctic vapor during the positive AD phase has been attributed to decreases in sea ice extent<sup>26,32</sup> altering the surface albedo and potentially enhancing the warming effect. We find that enhanced vapor from eastern Eurasia is promoted during several extreme positive AD events. However, despite the resemblance between the positive phase of the AD and the circulation anomalies that promote vapor from Eurasia to the Sector 5 side of the Arctic, our CESM simulation does not show strong correlation between AD years and positive/negative land vapor anomalies in Sector 5 (Supplementary Figs. 5a and 17b). This likely suggests that only certain manifestations (e.g., positioning) of the pressure anomalies associated with the positive AD, of which there are several<sup>30</sup>, promotes enhanced moisture export from Siberia to Sector 5. Additionally, as noted earlier, while the positive phase of the AD

may provide optimal circulation features for enhanced poleward land vapor transport, other anomalous circulation conditions can have a similar effect on land vapor transport, and these patterns should be explored in further detail in future studies.

The results presented here also suggest atmospheric circulation patterns have the largest control on land vapor anomalies in the Arctic, though ET anomalies play an important role as well. For both the high and low Arctic land vapor cases, the ET anomalies are modest and spatially heterogeneous across much of the four main contributing land regions (Figs. 9f and 10f). These findings indicate that atmospheric circulation patterns largely control summer Arctic land vapor while ET is a secondary control. However, there are instances where ET fluctuations have a notable impact on Arctic land vapor. The year with the highest concentration of EER vapor (year 3) is almost exclusively a result of anomalously high ET given the lack of poleward atmospheric circulation. Additionally, in the high Arctic land vapor case (Fig. 9), the atmospheric circulation patterns do not promote enhanced moisture flux from WNA, ENA, or WER. However, each of these regions have minor increases in Arctic land vapor contributions. This is likely the result of positive ET anomalies across much of Alaska, eastern Canada, and Europe. Therefore, monitoring large ET fluxes for land surfaces higher than 45°N, irrespective of the atmospheric circulation conditions, may offer additional insight into summer Arctic vapor and warming. The positive land vapor anomalies from these three regions are considerably lower than that of EER and CER despite similar ET patterns in all regions. This further underscores the importance of atmospheric circulation as the primary control on Arctic land vapor totals.

It is important to note that while CESM1 simulates Arctic climate reasonably well, the vapor sourcing estimates presented here are based on a climate model simulation, rather than observational/reanalysis data. Moisture source identification and tracking is a powerful tool for understanding climate linkages between remote regions, but presently, there are tradeoffs inherent to all tracking methods<sup>22</sup>. While the use of online numerical tracers in CESM1 removes all uncertainties related to the tracking algorithm (unlike back trajectory and 2D analytical models), the climate upon which the tracking is applied may (and does) have biases. Future implementation of moisture tracking algorithms in other earth system models will provide a necessary quantification of the uncertainties in moisture sourcing and tracking due to simulated climate state differences.

Previous work has identified the role of ocean-based evaporation and subsequent moisture transport in shaping Arctic water vapor<sup>16</sup>. In our simulation, the summer climatological oceanic vapor averaged across the Arctic is  $\sim 5.1 \text{ kg m}^{-2}$  with a variance of  $0.04 \text{ (kg m}^{-2})^2$ . While the variability of oceanic vapor can alter Arctic vapor concentrations, summer land-based vapor is 60% more variable over the course of this simulation. The climate model-based moisture tracking analysis presented here highlights the key role that terrestrial sources have in shaping summer Arctic vapor and warming patterns. These findings suggest land surface changes altering summer ET flux could have major implications for Arctic sea-ice and warming.

## METHODS

### Model setup

We use the Community Earth System Model version 1.3 (CESM1.3) (Meehl et al., 2019), which is an updated version of CESM1.2<sup>33</sup>. CESM1.3 is configured with the Community Atmosphere Model version 5 (CAM5) and the Community Land Model version 4 with the carbon-nitrogen model activated (CLM4CN). Both CAM5 and CLM4CN are run on a  $1.9^\circ \times 2.5^\circ$  finite volume grid. CAM5 is run with 30 active atmospheric levels in a hybrid-sigma pressure coordinate system. We run the land-atmosphere coupled simulation for 30 years. The ocean boundary conditions consist of prescribed monthly varying sea-surface temperatures (SSTs) and sea-ice

concentrations (SICs) taken from an existing equilibrated fully-coupled preindustrial simulation using CESM1.3<sup>34</sup>. By allowing these quantities to vary by month, we are able to capture SST and SIC-driven variability in the Arctic. We use the last 29 years for analysis and discard the first year to allow the atmosphere and water tracers (see below) to spin-up.

### Numerical water tracers

The atmosphere model (CAM5) used in this study has online water tracing capabilities<sup>35,36</sup>. A detailed description of how CAM5 traces water in the atmosphere can be found in Nusbaumer et al.<sup>37</sup>; a brief description of the process and how it compares to other water tracing methods is provided here. The model tracks the movement and transformation (phase changes) of evaporated moisture from a predetermined “tagged” region over a land or ocean surface until it precipitates out of the atmosphere. Upon evaporation (including transpiration) from a grid cell, moisture is assigned a tag corresponding to the region from which it evaporated. The tagged moisture (or “water tracer”) is advected horizontally and vertically through the atmosphere just as the standard (total) moisture is advected in the model. Tendencies for the tagged water (vapor, liquid, and ice) are calculated for the convective (shallow and deep), boundary layer, and cloud processes in the same way they are for standard water. As such, the tagged water undergoes all the same processes that regular moisture within the model does.

The water tracers are passive and have no effect on the climate system, so an arbitrary number of tracers can be implemented. Through implementing multiple water tracers from different tagged regions, we can directly quantify the contribution of different land and ocean surface regions to the Arctic vapor concentrations. Specifically, in this study, we track moisture originating from the land surface (all land grid cells), North Pacific (30°N – 70°N, 105°E – 100°W), North Atlantic (30°N – 70°N, 100°W – 75°E), Subtropical North Pacific (10°N – 30°N, 105°E – 100°W), Subtropical North Atlantic (10°N – 30°N, 100°W – 25°E), and the Arctic (>70°N) oceans (note, only ocean grid points within these domains are used). The land surface is divided into specific latitude and longitude bands to determine where land moisture is sourced from during the summer months. The high latitudes (HIL) are defined as greater than 60°N, the high-mid latitudes (HML) between 60°N and 45°N, the low-mid latitudes (LML) between 45°N and 30°N, and the low latitudes (LOL) between 30°N and 0°. The Northern Hemisphere land surface is further split into five longitude regions, all defined between 30°N and 90°N. western North America (WNA) is defined between 170°W and 105°W, eastern North America (ENA) between 105°W and 15°W, western Eurasia (WER) between 15°W and 45°E, central Eurasia (CER) between 45°E and 105°E, and eastern Eurasia (EER) between 105°E and 170°W. A map view of these regions is provided in Fig. 2.

The primary advantage of tracking atmospheric moisture with online numerical water tracers over other tracking methods derives from the fact that the water tracers are embedded within the climate model itself. The prognostic nature of the online tracers removes the need to make simplifying assumptions regarding the influence of sub-grid processes, such as convection, cloud microphysics, and turbulence, on the tagged moisture concentrations, which are required for offline tracking methods, such as Lagrangian back trajectory analyses, and two-dimensional analytical models<sup>22</sup>. Previous tracking method intercomparisons have shown that these simplifying assumptions, such as the “well-mixed” assumption to distribute evaporation vertically in the atmospheric column in analytical models, and the arbitrary thresholds used to diagnose regions of moisture uptake along back trajectories in Lagrangian models, can bias the identification of moisture source regions<sup>38–40</sup>.

### Statistical significance

In Section “Controls on Total Arctic Land Vapor”, we identify the three summers with the largest and three summers with the smallest Arctic concentrations of water vapor sourced from the land surface (0.9 and 0.1 quantiles). We then quantify the anomalous contributions to Arctic water vapor from the different tagged regions in those 3-year subsets, and assess whether those region-specific anomalous contributions are statistically significant with the use of a bootstrap resampling method. Specifically, the mean of a region’s water vapor contribution from the three-year subset is compared to the mean of 10,000 3-year subsets from that region sampled randomly with replacement from the 29-year

simulation (null distribution). If the mean of the 3-year subset falls outside the 2.5–97.5 percentile distribution of the 10,000 resamples, then the null hypothesis is rejected and the contribution is marked as statistically significant.

### ERA5 reanalysis data

To evaluate the model performance in simulating Arctic climate, we compare the vertically integrated water vapor and temperature with ERA5 monthly atmospheric reanalysis data<sup>41</sup>. The reanalysis data is archived at a 0.25°x0.25° resolution and is re-gridded to a 1.9°x2.5° resolution to match that of CESM. Since integrated vapor is discontinuous in portions of the Arctic (particularly around the Greenland landmass), the re-gridding is performed using a patch interpolation method<sup>42</sup> rather than using a method like bilinear interpolation. ERA5 data from the years 1990–2018 are averaged to create a 29-year sample to compare to the CESM simulation data.

### DATA AVAILABILITY

All model output used in this manuscript are available from the corresponding author upon reasonable request.

### CODE AVAILABILITY

All code used in this manuscript is available from the corresponding author upon reasonable request.

Received: 30 November 2020; Accepted: 26 March 2021;

Published online: 21 April 2021

### REFERENCES

- Masson-Delmotte, V. et al. Global Warming of 1.5°C. An IPCC Special Report on the impacts of global warming of 1.5°C above pre-industrial levels and related global greenhouse gas emission pathways, in the context of strengthening the global response to the threat of climate change, sustainable development, and efforts to eradicate poverty (IPCC, 2018).
- Kelly, P. M., Jones, P. D., Sear, C. B., Cherry, B. S. G. & Tavakol, R. K. Variations in Surface Air Temperatures: Part 2. Arctic Regions, 1881–1980. *Mon. Weather Rev.* **110**, 71–83 (1982).
- Bintanja, R. & van der Linden, E. The changing seasonal climate in the Arctic. *Sci. Rep.* **3**, 1556 (2013).
- Kurtz, N. T., Markus, T., Farrell, S. L., Worthen, D. L. & Boisvert, L. N. Observations of recent Arctic sea ice volume loss and its impact on ocean-atmosphere energy exchange and ice production. *J. Geophys. Res.* **116**, C04015 (2011).
- Kwok, R. & Untersteiner, N. The thinning of Arctic sea ice. *Phys. Today* **64**, 36–41 (2011).
- Lang, A., Yang, S. & Kaas, E. Sea ice thickness and recent Arctic warming. *Geophys. Res. Lett.* **44**, 409–418 (2017).
- Lindsay, R. W. & Zhang, J. The thinning of Arctic sea ice, 1988–2003: have we reached the tipping point? *J. Clim.* **18**, 4879–4894 (2005).
- Dai, A. et al. Arctic amplification is caused by sea-ice loss under increasing CO<sub>2</sub>. *Nat. Comm.* **10**, 121 (2019).
- Screen, J. A. & Simmonds, I. Increasing fall-winter energy loss from the Arctic Ocean and its role in Arctic temperature amplification. *Geophys. Res. Lett.* **37**, L16707 (2010).
- Serreze, M. C. & Francis, J. A. The Arctic amplification debate. *Clim. Change* **76**, 241–264 (2006).
- Kapsch, M., Graverson, R. & Tjernström, M. Springtime atmospheric energy transport and the control of Arctic summer sea-ice extent. *Nat. Clim. Change* **3**, 744–748 (2013).
- Mortin, J. et al. Melt onset over Arctic sea ice controlled by atmospheric moisture transport. *Geophys. Res. Lett.* **43**, 6636–6642 (2016).
- Serreze, M. & Barry, R. Processes and impacts of Arctic amplification: a research synthesis. *Glob. Planet. Change* **77**, 85–96 (2011).
- Ghatak, D. & Miller, J. Implications for Arctic amplification of changes in the strength of the water vapor feedback. *J. Geophys. Res. Atmos.* **118**, 7569–7578 (2013).
- Zhong, L., Hua, L. & Luo, D. Local and external moisture sources for the Arctic warming over the Barents–Kara Seas. *J. Clim.* **31**, 1963–1982 (2018).
- Jakobson, E. & Vihma, T. Atmospheric moisture budget in the Arctic based on the ERA-40 reanalysis. *Int. J. Clim.* **30**, 2175–2194 (2010).

17. Dufour, A., Zolina, O. & Gulev, S. K. Atmospheric moisture transport to the Arctic: assessment of reanalyses and analysis of transport components. *J. Clim.* **29**, 5061–5081 (2016).
18. Luo, B., Luo, D., Wu, L., Zhong, L. & Simmonds, I. Atmospheric circulation patterns which promote winter Arctic sea ice decline. *Environ. Res. Lett.* **12**, 054017 (2017).
19. Gimeno, L., et al. Atmospheric moisture transport and the decline in Arctic Sea ice. *WIREs Clim. Change*. **10**, <https://doi.org/10.1002/wcc.588> (2019).
20. Gimeno, L., Vázquez, M., Nieto, R. & Trigo, R. M. Atmospheric moisture transport: the bridge between ocean evaporation and Arctic ice melting. *Earth Syst. Dyn.* **6**, 583–589 (2015).
21. Vázquez, M., Nieto, R., Drumond, A. & Gimeno, L. Moisture transport into the Arctic: source-receptor relationships and the roles of atmospheric circulation and evaporation. *J. Geophys. Res. Atmos.* **121**, 13493–13509 (2016).
22. Gimeno, L. et al. Oceanic and terrestrial sources of continental precipitation. *Rev. Geophys.* **50**, RG4003 (2012).
23. Zhang, Y. et al. Multi-decadal trends in global terrestrial evapotranspiration and its components. *Sci. Rep.* **6**, 19124 (2016).
24. Zhu, Z. et al. Greening of the Earth and its drivers. *Nat. Clim. Change* **6**, 791–795 (2016).
25. Middlemas, E. A., Kay, J. E., Medeiros, B. M. & Maroon, E. A. Quantifying the influence of cloud radiative feedbacks on Arctic surface warming using cloud locking in an Earth system model. *Geophys. Res. Lett.* **47**, e2020GL089207 (2020).
26. Wang, J. et al. Is the Dipole Anomaly a major driver to record lows in Arctic summer sea ice extent? *Geophys. Res. Lett.* **36**, L05706 (2009).
27. Wu, B., Wang, J. & Walsh, J. E. Dipole Anomaly in the winter Arctic atmosphere and its association with sea ice motion. *J. Clim.* **19**, 210–225 (2006).
28. Skeie, P. Meridional flow variability over the Nordic Seas in the arctic oscillation framework. *Geophys. Res. Lett.* **27**, 2569–2572 (2000).
29. Watanabe, E., Wang, J., Sumi, A. & Hasumi, H. Arctic dipole anomaly and its contribution to sea ice export from the Arctic Ocean in the 20th century. *Geophys. Res. Lett.* **33**, L23703 (2006).
30. Kapsch, M., Skific, N., Graversen, R. G., Tjernström, M. & Francis, J. A. Summers with low Arctic sea ice linked to persistence of spring atmospheric circulation patterns. *Clim. Dyn.* **52**, 2497–2512 (2019).
31. Rinke, A. et al. Trends of vertically integrated water vapor over the Arctic during 1979–2016: consistent moistening all over? *J. Clim.* **32**, 6097–6116 (2019).
32. Hegyi, B. M. & Taylor, P. C. The regional influence of the Arctic Oscillation and Arctic Dipole on the wintertime Arctic surface radiation budget and sea ice growth. *Geophys. Res. Lett.* **44**, 4341–4350 (2017). (2017).
33. Hurrell, J. W. et al. The community earth system model: a framework for collaborative research. *Bull. Am. Meteor. Soc.* **94**, 1339–1360 (2013).
34. Zhu, J. et al. Reduced ENSO variability at the LGM revealed by an isotope-enabled Earth system model. *Geophys. Res. Lett.* **44**, 6984–6992 (2017).
35. Brady, E. C. et al. The connected isotopic water cycle in the community earth system model version 1. *J. Adv. Model. Earth Syst.* **11**, 2547–2566 (2019).
36. Nusbaumer, J. & Noone, D. Numerical evaluation of the modern and future origins of atmospheric river moisture over the West Coast of the United States. *J. Geophys. Res. Atmos.* **123**, 6423–6442 (2018).
37. Nusbaumer, J., Wong, T., Bardeen, C. & Noone, D. Evaluating hydrological processes in the Community Atmosphere Model Version 5 (CAM5) using stable isotope ratios of water. *J. Adv. Model. Earth Syst.* **9**, 949–977 (2017).
38. Sodemann, H., Schwierz, C. & Wernli, H. Interannual variability of Greenland winter precipitation sources: Lagrangian moisture diagnostic and North Atlantic Oscillation influence. *J. Geophys. Res. Atmos.* **113**, D03107 (2008).
39. van der Ent, R. J., Tuinenburg, O. A., Knoche, H. R., Kunstmann, H. & Savenije, H. H. G. Should we use a simple or complex model for moisture recycling and atmospheric moisture tracking? *Hydrol. Earth Syst. Sci.* **17**, 4869–4884 (2013).
40. Dominguez, F., Miguez-Macho, G. & Hu, H. WRF with water vapor tracers: a study of moisture sources for the North American Monsoon. *J. Hydro.* **17**, 1915–1927 (2016).
41. Hersbach, H. et al. The ERA5 global reanalysis. *Quart. J. Roy. Meteor. Soc.* **146**, 1999–2049 (2020).
42. Khoei, A. R. & Gharehbaghi, S. A. The superconvergence patch recovery technique and data transfer operators in 3D plasticity problems. *Fin. Elem. Anal. Des.* **43**, 630–648 (2007).

## ACKNOWLEDGEMENTS

The CESM project is supported primarily by the National Science Foundation (NSF). This material is based upon work supported by the National Center for Atmospheric Research, which is a major facility sponsored by the NSF under Cooperative Agreement No. 1852977. Computing and data storage resources, including the Cheyenne supercomputer (<https://doi.org/10.5065/D6RX99HX>), were provided by the Computational and Information Systems Laboratory (CISL) at NCAR. We thank all the scientists, software engineers, and administrators who contributed to the development of CESM1.

## AUTHOR CONTRIBUTIONS

T.S.H. and C.B.S. designed the study; C.B.S. and J.Z. set up the simulation; T.S.H. performed the analysis; T.S.H. and C.B.S. wrote the manuscript. All authors reviewed and edited the manuscript.

## COMPETING INTERESTS

The authors declare no competing interests.

## ADDITIONAL INFORMATION

**Supplementary information** The online version contains supplementary material available at <https://doi.org/10.1038/s41612-021-00181-y>.

**Correspondence** and requests for materials should be addressed to T.S.H.

**Reprints and permission information** is available at <http://www.nature.com/reprints>

**Publisher's note** Springer Nature remains neutral with regard to jurisdictional claims in published maps and institutional affiliations.



**Open Access** This article is licensed under a Creative Commons Attribution 4.0 International License, which permits use, sharing, adaptation, distribution and reproduction in any medium or format, as long as you give appropriate credit to the original author(s) and the source, provide a link to the Creative Commons license, and indicate if changes were made. The images or other third party material in this article are included in the article's Creative Commons license, unless indicated otherwise in a credit line to the material. If material is not included in the article's Creative Commons license and your intended use is not permitted by statutory regulation or exceeds the permitted use, you will need to obtain permission directly from the copyright holder. To view a copy of this license, visit <http://creativecommons.org/licenses/by/4.0/>.

© The Author(s) 2021